Flexible unsupervised binary change detection algorithm identifies phase transitions in continuous image streams

Paul Chao[1], Xianghui Xiao[2], and Ashwin J. Shahani *[1]

[1]Department of Materials Science and Engineering, University of Michigan, Ann Arbor, MI 48109

[2]National Synchrotron Light Source II (NSLS-II), Brookhaven National Laboratory, Upton, New York 11973

* shahani@umich.edu, (734) 764-5648

December 22, 2020

Abstract

Sequences of projection images collected during *in-situ* tomography experiments can capture the formation of patterns in crystallization and yield their three-dimensional growth morphologies. These image streams generate enormous and high dimensional datasets that span the full extent of a phase transition. Detecting from the continuous image stream the characteristic times and temperatures at which the phase transition initiates is a challenge because the phase change is often swift and subtle. Here we show a flexible unsupervised binary classification algorithm to identify a change point during data intensive experiments. The algorithm makes a prediction based on statistical metrics and has a quantifiable error bound. Applied to two *in-situ* X-ray tomography experimental datasets collected at a synchrotron light source, the developed method can detect the moment at which the solid phase emerges from the parent liquid phase upon crystallization and without performing computationally expensive volume reconstructions. Our approach is verified using a simulated X-ray phantom and its performance evaluated with respect to solidification parameters. The method presented here can be broadly applied to other big data problems where time series can be classified without the need for additional training data.

Keywords: Solidification, nucleation, machine learning, sinogram, x-ray tomography

Acknowledgment

We gratefully acknowledge financial support from the National Science Foundation (NSF) CAREER program under Award No. 1847855. We thank Dr. Insung Han, Dr. Saman Moniri, Dr. Caleb Reese, Dr. Riddhiman Bhattacharya, and Dr. Nancy Senabulya for assisting in the synchrotron-based experiment; and Pavel Shevshenko for assistance in sample preparation. This research used resources of the Advanced Photon Source, a U.S. Department of Energy (DOE) Office of Science User Facility operated for the DOE Office of Science by Argonne National Laboratory under Contract No. DE-AC02–06CH11357.

1 Introduction

All technological materials start their lifetimes in the liquid phase. The liquid to solid phase transformation during the cooling of liquid metallic alloys begins at temperatures slightly below the melting (or liquidus) temperature of the alloy. For discontinuous transformations, the initiating process is nucleation, which is associated with metastability, *i.e.*, the existence of an energy barrier and the occurrence of a rare but large energy fluctuation [1]. The magnitude of this barrier depends on the alloy composition and solid-liquid interface free energy [2, 3]. Though we have achieved substantial understanding of the ensuing crystal growth process, the initial solid evolution has been difficult to quantify experimentally as nucleation unfolds too rapidly to discern at small spatial scales.

Recent advancements in X-ray microscopy to non-destructively probe the internal microstructure of materials in three-dimensions down to micrometers and even nanometers in length-scale (see Ref. [4, 5, 6] and references therein), coupled with high brightness X-ray radiation at third generation synchrotron light sources and fast detector acquisition, have opened the doors to *in-situ* X-ray tomography (XRT). During these experiments, large amounts of 4D (3D space plus time resolved) imaging data record the transformation of materials under external stimuli such as heat, mechanical loading, *etc.* [7, 6, 8]. For example, the crystallization behavior of alloys can be studied at varying time points, providing detailed snapshots of the growth process as it transpires [9, 10].

In attenuation-contrast tomography, the sample is imaged in transmission, see **Figure 5(a)**. Typically, *in situ* crystallization experiments are done by cooling (or heating) the sample in a furnace while X-ray projections are recorded in parallel. Slow and controlled cooling to a temperature below the liquidus provides a thermodynamic driving force (undercooling) that is necessary to overcome the aforementioned nucleation barrier. The resultant data size is primarily dependent on the experiment time as well as the detector fidelity, frame rate, and size. For reference, a single tomographic scan (where the sample rotates from 0 to 180°) consisting of 2000 projections from a 5 megapixel detector is over 3 GB in size. Therefore, collecting an image stream while continuously rotating the sample for 10 full rotations would yield 60 GB and 100 full rotations would yield over half a TB of data, begetting the term "Big Data" [11]. As a result, there is a rising need for machine learning tools to explore and extract relevant information from these large digital datasets. Manual processing is impractical, as far as nucleation is concerned: Searching for nucleation events within a vast 4D domain is equivalent to finding the proverbial "needle in a haystack."

Currently, knowledge of phase equilibria provides some rough guidance on when nucleation will occur and thus when to begin recording the data. Yet this approach fails when the materials system is not well characterized and its phase equilibria not defined (*e.g.*, some quasicrystal-forming alloys [12]); when crystallization proceeds far-from-equilibrium, which is often the norm and not the exception [13]; or when there exist several competing allotropes [14]. Therefore, considerable data processing after the experiment is needed to reconstruct the data and identify (often by visual inspection) the sequence of projection images corresponding to the phase transition of inter-

est. Reconstruction, however, is computationally intensive and time-consuming, as a number of parameters require sample-specific tuning [15, 16]. Recently, a machine learning approach has been presented by Liotti et al. to identify crystal nucleation events in X-ray image sequences; they were able to train a computer vision algorithm to evaluate the Big Data and thus quantify the nucleation undercooling and nucleation rate [17]. Similar to their approach, our method can resolve individual nucleation events, thus offering a higher granularity of analysis compared to other methods involving thermocouples, which instead measure average properties of an ensemble of nuclei. Nevertheless, our approach diverges from that of Liotti et al. in that we do not use deep neural networks which require training images to identify crystal nuclei in the image.

This general problem of crystal detection resides in the field of time series classification algorithms, a sub-field of machine learning [18, 19]. Here we showcase an algorithm that directly analyzes changes in an image stream acquired during *in-situ* XRT of alloys during crystallization and classifies the time series as either a *liquid* state or *liquid* + *solid* state. Changes in these experiments can be the phase composition, crystal size, or other measurable quantities. This binary classification algorithm is designed to be unsupervised (*i.e.*, not requiring training data) and is aimed to be a rapid method to pinpoint the onset of phase transition temporally. Our algorithm is inspired by recent work in the computational chemistry community to classify self assembly pathways; as in Ref. [20], we utilize simple statistical measures to describe the pixel data in each projection image. We demonstrate that this information is more than sufficient to predict the nucleation temperature, with an accuracy of ±2 °C from all datasets considered.

Armed with our algorithm, a researcher can conduct multiple experiments at various heating/cooling rates and use the results to generate transformation diagrams. Additionally, the remarkable ability of the algorithm to detect subtle changes provides a simple solution to broad challenges in the interpretation of image stream data.

2 Methods

2.1 Experimental

All XRT studies were done at sector 2-BM at the Advanced Photon Source (APS) at Argonne National Laboratory in Lemont, Illinois, United States. Using a furnace with X-ray transparent windows, the sample was first held above the liquidus temperature for approximately five minutes, to ensure melting and homogenization. The molten alloy sample was protected by a thin oxide skin naturally grown by thermal oxidation. Once fully melted, the sample was then cooled continuously for one hour at a rate of 1 K/min. At the same time, X-ray projections were recorded at a rate of 50 Hz using a polychromatic "pink" beam centered at 27 keV, and a PCO Edge 5.5 CMOS camera that was optically coupled to a 20 µm LuAg:Ce scintillator. Tomographic data was processed within TomoPy [15], a Python based open source function package. The Gridrec algorithm [21], a direct Fourier-based method, was used to reconstruct the data

and in turn, validate the performance of our computational protocol.

2.2 Algorithm

The classification algorithm was implemented in Python [22] using open-source libraries scikit-learn [23], numpy [24], and others. The three-dimensional array of the projected data was stored and managed in a HDF [25] container that was processed by the algorithm. The projection data referenced here in this paper are freely available [26, 27]. The three-step procedure is outlined and explained in the context of the first experimental dataset, see Sec. 3.2. Codes to reproduce the results are open source and also are available online [28] on github.

The procedure to create the simulated phantoms is detailed in Sec. 3.4. We considered the isothermal, diffusion-limited growth of a solid sphere in a binary alloy. The supersaturation changes with time until it is finally zero and growth is finished. Under these conditions, the solid growth rate can be found analytically [29]. We used MATLAB [30] to construct the phantoms and calculate the forward projections of the solidification process, which were then fed into our three-step procedure. More details can be found in **Supplemental Information 6.5**. Codes related to the algorithm are available upon request, including those to generate X-ray phantoms of the solidification process.

3 Results

3.1 Algorithm description

Our approach can be broken down into 3 general parts: Firstly, the image stream is pre-processed to normalize and remove any speckle noise. Secondly, various statistical metrics are calculated for each independent time step. The following examples will demonstrate how deviations in statistical metrics serve as basic signatures of the phase transition. Thirdly, fuzzy clustering is performed on the resulting data compressed into two principal components and a time axis. Our algorithm does not require *a priori* knowledge or user input; that said, it can be refined through the degree of data pre-processing, selection of metrics, and also parameterization of fuzzy clustering. Each of these steps will be expanded upon in the context of the experimental dataset presented below.

3.2 Case study #1: Formation of quasicrystals

The formation of quasicrystals has been a longstanding puzzle in condensed matter physics [31]. To this end, XRT is a novel tool that can provide fresh insight into the solidification behavior. The first step in our data-driven discovery is to identify the critical point at which quasicrystals nucleate from a liquid, which is important for understanding the influence of icosahedral short range order on the relative undercooling [32, 33]. Ref. [12] was among the first to capture in 3D the growth of a thermodynamically-stable Al-9.55at%Ni-9.55at%Co quasicrystal from a liquid melt. Their data (1.4 TB in volume) serves as a first proof-of-concept for our algorithm. Determination of the nucleation time and temperature was verified in a 'brute force' way by reconstructing successive tomographic volumes, as mentioned above. Below, we present step-by-step our change point detection algorithm in the context of this dataset.

The Big Data in the form of a three-dimensional array (180,001×800×2,560 pixels in size) with each value stored in an HDF container as a 16-bit unsigned integer. The first and largest dimension is the number of projections, which can be correlated to a specific sample rotation angle and time during the experiment. For each 180° rotation of the sample, 1,000 projections were taken with an exposure time of 14 ms for a total of 90 full sample rotations. Simultaneously, the sample was cooled from 1293 K at a rate of 1 K/min. 3D reconstructions provided some guidance that quasicrystals nucleate from the liquid phase at temperatures around 1260 K. Each projection consisted of 2560×800 pixels in the row and column of the digital detector, respectively. From the projection data we constructed a *sinogram*, which includes a single row of pixels from every projection; there are thus a total of 800 sinograms that are each 180,001×2,560 pixels in size. The sinogram represents the data collected for a single 'slice' of the sample across all view angles. It is used by our algorithm to identify the change point at a given cross-section of our sample. The data collection and data morphology are illustrated in **Figure 5(a)**.

The dominant contrast mechanism in our experiments is photoabsorption, wherein the pixel values on the detec-

tor indicate the attenuation of X-radiation due to the X-ray-sample interaction [34]. Generally, the intensity of the transmitted beam depends on a number of factors, including material composition, density, and thickness [34, 35]. According to the Beer-Lambert law, $I(x,y)/I_0(x,y) = \mathrm{Exp}(-\int_l \mu(x,y,z)\, dz)$, the ratio of transmitted (I) to incident (I_0) beam intensity for each x and y coordinate of the detector plane scales exponentially with the linear attenuation coefficient of the material (μ) and the material thickness (l) along the beam path (z); for a constant thickness, the integrated attenuation coefficient can be extracted by taking the negative logarithm of the recorded intensity [4]. This procedure is done when constructing the sinogram. As a result, the pixel intensity in the sinogram is indicative of its phase (*i.e.*, liquid, solid, *etc.*) for a diffusive (or non-congruent) transformation. For instance, in this particular alloy, the solid quasicrystal is richer in the heavy elements Ni and Co compared to the solute-depleted liquid.

Prior to quantifying statistical trends in the sinogram, we must first remove extraneous noise (*e.g.*, high energy photons, dead detector pixels, *etc.*) by performing normalization and low pass filtering. The former involves subtracting the 'initial condition' – in our case, the liquid portion of the sinogram (*i.e.*, the projections from the first 360° sample rotation during which the entire sample is still in liquid state or untransformed) – from the remaining projections. The result of this procedure is presented in **Figure 5(b)**. The second step is to downsample the sinogram by summing pixels in a n×n square neighborhood. This procedure not only eliminates noise but also reduces the data size and increases analysis speed; a factor of 10× downsampling maintains the best speed gain without distorting the data, see **Supplementary Figure 6.1**. In that figure, we show the detected nucleation point with respect to the percent of downsampling. It is worth noting that the degree of downsampling (ranging from 10× to 100×) does not change appreciably the detected change point. For example, by downsampling by a factor of 100× and more, the estimated change point is within a ±5 °C temperature range. The downsampled result is further discretized to 256 levels within the maximum and minimum pixel intensity.

At this point, it is visually apparent in the pre-processed sinogram in **Figure 5(b)** when the solid phase has nucleated. This data will be our input for the algorithm. For each column (time-step or projection-number) of the sinogram (totalling 180,001 time-steps or projections) we calculate a number of statistical metrics as illustrated in **Figure 5**: these are the number of maximum values, number of minimum values, mean values, standard deviation, number of unique pixel values, and other measures of central tendency. The metrics we chose are not representative of the exhaustive possibilities. Rather, they are simple to implement and are the minimum necessary to detect change points (as will be demonstrated below).

These metrics are then standardized by centering and scaling to unit variance to prevent misinterpretation after principal component analysis [23]. Linear principal component analysis (PCA) on the statistical metrics captures and projects the largest variances in each metric onto the orthogonal principal component axis [36]. We then cluster the data projected into the two component PCA with a third dimension indicates time (or equivalently projection number), see **Figure 5(a)**. We separate the data into two clusters: *before* and *after* quasicrystal formation. **Figure 5(b)** shows a

projection of the clustered data into the two component PCA space. We include in this figure the biplot showing the direction and magnitude each metric imposes on the two-component PCA plot. The Scree plot demonstrates that two components capture 87.96% of the variance, see **Supplemental Information 6.2**.

Of the many cluster separation algorithms in unsupervised machine learning, the vast majority separate the data discretely into one cluster or another [23, 37, 38]. However, nucleation is a stochastic phenomenon (*i.e.*, dependent on random fluctuations) and so even in two identical systems, it will occur at slightly different times. Therefore, we seek an alternative method to partition our data in light of this uncertainty. To this end, we utilize fuzzy c-means clustering [23, 39] to distinguish between *liquid* and *liquid + solid* regimes in the sinogram. Uncertainty of the separation interface is determined by the fuzzy partition coefficient (1.8), which is generally recommended to lie in the interval of [1.5, 2.5] [40]. The coefficient controls the amount of membership overlap between clusters; larger values correspond to greater overlap between the clusters and a higher degree of imprecision whereas smaller values will result in distinct clusters with less overlap between clusters. **Figure 5(c)** illustrates the results from fuzzy clustering. The intersection of the two membership probabilities, *i.e.*, the maximum of the product of the two membership probabilities, is the estimated critical point of nucleation. Additionally, we can use the probability assigned by the fuzzy clustering to estimate the time bounds around the critical event.

For the time interval determined by a probability greater than 60% belonging to each cluster, the critical point was calculated to be between 804 seconds and 902 seconds into the data acquisition, corresponding to a temperature window of 1259.8 K to 1258.2 K, respectively, during continuous cooling. This estimate agrees with our visual observation of the sinogram as well as the ground-truth reconstructions (**Supplemental Information 6.3**), which indicate that quasicrystal growth commences after 800 seconds elapsed, corresponding to a temperature of 1260 K [12]. Compared to the phase diagram of the Al-Ni-Co system [41], this temperature corresponds to a nucleation undercooling of 17.5 K (referenced against the equilibrium liquidus temperature).

3.3 Case study #2: Formation of primary silicon in a chemically-modified alloy

The nucleation and growth pathway of faceted silicon particles from the melt can be influenced by the addition of trace impurity elements such as strontium. Here, too, we investigate the solidification behavior *via* 4D XRT, focusing on an Al-7at%Cu-35at%Si-0.03at%Sr alloy [42]. Below the Si liquidus, the system should exist in the form of a nearly-pure solid Si phase plus a Cu- and Sr-enriched liquid phase. Our goal is to identify the critical point at which the solid Si nucleates from the liquid, and this dataset presents a second validation of the algorithm's performance with more subtle contrasting agents as well as slower growth rates. The reduced growth rate in comparison to the quasicrystal can be attributed to thermodynamic and kinetic reasons: thermodynamically, the liquidus curve in the phase diagram is steeper, therefore for a unit temperature decrease, the solid phase's volume fraction increase is minimal [41, 43].

From a kinetic standpoint, the Si is highly faceted [42] unlike the atomically rough quasicrystals [33]. Thus there is a kinetic limitation for the incorporation of atoms/clusters to the flat interfaces.

The experimental data are in the form of a 3D array of size (120,001×800×2,560 pixels) with each pixel stored as a 32-bit unsigned integer (totaling 457 GB). Similar to the above case, the first dimension represents the number of projections collected during 40 full stage rotations of the sample. That is, we acquired 1,500 projections for each 180° rotation. We used an exposure of 14 ms and each full rotation took 42 seconds. We began the data acquisition as we lowered the furnace temperature from 1207 K to 1167 K at a rate of 1 K/min.

Benchmark reconstructions showing the growth of solid Si from the liquid melt are provided in the **Supplementary Information 6.4**. In this instance, there are two Si crystals that nucleate heterogeneously from the oxide film containing the sample and grow at a rate of 0.03 µm/s. This dataset is obtained in a similar fashion to the first with the exception that the absorption contrast between the two phases comes from the minor Cu species in the melt; we note the concentration of Sr in the alloy is too minor to contribute to X-ray attenuation; and Al and Si have nearly equal attenuation coefficients [44]. Additionally, there is increased noise in the dataset that we attribute to beam motion from small vibrations to the X-ray optics [45]. Despite these challenges, our algorithm can still identify the onset of Si crystallization, see the results of PCA analysis and clustering in **Figure 5**.

Assuming a probability greater than 60% belonging to each cluster (similar to case #1 above), the critical point was calculated to be between 1278 seconds and 1446 seconds into the acquisition, corresponding to a temperature window of 1185.7 K to 1182.9 K, respectively. This estimate agrees with the ground-truth reconstructions (**Supplemental Information 6.4**), which indicate that the Si growth commences after 1350 seconds has elapsed, corresponding to a temperature of 1185 K [42]. Compared to the liquidus temperature from calculated phase diagrams from the Thermo-Calc database TTAL6 [46], this temperature corresponds to a nucleation undercooling of 22.5 K.

3.4 Validation on synthetic phantoms

To better understand the sensitivity and performance of our computational protocol, we simulated the solidification process, specifying the exact moment of crystallization and comparing to predictions from the algorithm. This allows us to systematically test the influence of solidification parameters on the performance of the algorithm and explain possible discrepancies between results on future experimental datasets. We simulate a 400 pixel diameter circular liquid area wherein the solid will nucleate and grow. In order to mimic the experimental data as closely as possible, we account for the time-varying supersaturation in a binary alloy which decays to zero at long times, following Ref. [29]. The full analytical solution of the diffusion equation is included in the **Supplemental Information 6.5**.

The input parameters for our simulation include the binary alloy composition, equilibrium partition coefficient, characteristic diffusion time, elemental attenuation coefficients, and data collection speed. Beginning with a homoge-

neous binary liquid alloy of predetermined composition, the nucleation event is 'seeded' by changing pixel values in a small, circular region within the liquid to the solid composition as described by the equilibrium partition coefficient. The nucleated solid then grows according the the user-scaled, analytically derived growth rate, see **Supplemental Information 6.5**. The liquid composition is then updated to maintain mass balance. At each time-step, the forward projection is calculated from a rotated phantom. In doing so, we invoke the Beer-Lambert law, generalized for a two-component system. The attenuation coefficients of the two components in this simulation are an order of magnitude different, although in principle any combination of attenuation coefficients would be acceptable since we normalize and re-scale pixel intensities in the sinogram (step #1 of our algorithm). The user-defined data collection speed dictates the number of evenly spaced projections recorded during a full revolution. For each simulation, we scaled the growth rate and subsequently passed each simulated result through our three-step algorithm to identify the point at which the solid phase nucleates from the liquid. This allows us to describe the algorithm's time sensitivity and gauge the fuzzy clustering boundaries.

Broadly, we find that the algorithm more accurately pinpoints the moment the phase transformation initialized for faster solidification rates, see **Figure 5(b)**. Using the same 60% cluster probability threshold, the simulation with solid growth 10× faster had a range of 23 time units with the estimated nucleation point 17 time units behind the actual point. For the same threshold, the slower simulation had a wider range of 46 time units with the calculated nucleation time delayed by 42 time units. The algorithm thus captures rapid dynamics more accurately with a smaller uncertainty window for the nucleation event.

4 Discussion

This work introduces an unsupervised binary classification algorithm applied to identification of critical events in continuous image streams, such as those produced from high-throughput characterization techniques like 'fast' X-ray tomography. We validate this algorithm with two experimental datasets and use simulations to explore the effect of solidification growth rate on the algorithm performance. The first experimental dataset shows a quasicrystal growing rapidly from the melt (owing to its atomically rough interfaces) [33]; moreover, it exhibits excellent absorption contrast between the liquid and solid phases. In contrast, the second dataset shows silicon particles that grow very slowly from the liquid under the same cooling rate (attributed, in part, to kinetic limitations of atom incorporation at the atomically flat {111} planes) [47]. Additionally, the latter dataset shows a comparatively weaker contrast between the two phases. In both cases, the method accurately estimates the time of nucleation within estimated time bounds. We can translate these results to nucleation undercoolings, as described in Sec. 3.2 - 3.3. We find a larger nucleation undercooling required for Si with respect to the quasicrystal, which most likely stems from the difference in the solid-liquid interfacial energies, approx. 0.1 J/m^2 and 0.01 J/m^2 (orders-of-magnitude), respectively, holding all else constant (including shape factors for heterogeneous nucleation). Interfacial energy is, in turn, influenced by the structural similarity between solid and liquid phases. In general, metallic liquids have an icosahedral short-range-order [33] which is why quasicrystals have a vanishingly small solid-liquid interfacial energy, and nucleate readily from the liquid phase.

Nevertheless, the accuracy of our approach is partially dependent on the growth rate of the nucleating phase and amount of data spanning the phase transformation. For instance, the quasicrystal grew to a maximal size (1067 µm in length in the analyzed cross-section) within 20 full tomographic rotations (25 min) whereas the Si crystal kept growing steadily to a maximal size of 211 µm in length in the analyzed cross-section until the end of data acquisition (20 min). In light of these two different average growth rates (0.2 µm/s for the former *vs.* 0.03 µm/s for the latter), and comparing the identified critical points for each experimental dataset, the algorithm more accurately predicts the onset of crystallization for the quasicrystal. Naturally, this is due to a sudden and distinct contrast change in the projection images, pre- and post-nucleation, which arises from the solute rejection in a noncongruent or diffusive transformation. That is, our algorithm is sensitive not to the critical nucleus itself but rather to its local environment (the liquid phase). Ultimately, we capture not the "needle from the haystack" (see Introduction) but instead *the hay displaced by the needle*. The change point is more accurately estimated when sufficient data from both the pre- and post- nucleation regimes are supplied for the fuzzy clustering algorithm. This is the trade-off between *complexity* (of the sheer amount of data so analyzed) and *accuracy* (of resolving the critical point), not uncommon to many learning problems. We note also that the above experimental results are consistent with our simulations. Evaluating the algorithm for conditions where all other variables are held constant, slower growth rate by a factor of 10 resulted in a delay of the detected

critical point by a factor of 2 and the window approximating the nucleation event is a factor of 2 larger for the slow growth simulation, both of which are to be expected. These trends suggest that the algorithm is especially amenable for phase transformations that proceed far-from-equilibrium, under high driving forces (and correspondingly high growth rates). Other simulation parameters such as the ratio of solid to liquid attenuation coefficients indeed changes the contrast in the sinogram but did not influence the algorithm's ability to estimate the change point. This is because the first step of the algorithm included a normalization procedure that equalizes the imposed contrast differences, as mentioned previously.

Looking ahead, the natural extension of our work is to implement our computational protocol during an *in-situ* experiment. The challenges of integrating it into the existing data collection schema for real time diagnosis will be addressed in a future study. Nonetheless, we can firstly use the algorithm to quickly screen for change points and nucleation characteristics, comparing different samples, as we did here. Secondly, we can use the output of the algorithm to down-select a time-interval suitable for reconstruction, instead of reconstructing all of the projection data in a continuous image stream. This approach offers considerable time-savings since one would not need to search through a vast reconstruction space for critical events. A third point (beyond making systematic comparisons and the scope of this paper) is that we can create time-temperature-transformation (TTT) diagrams to identify under what conditions nucleation is favored. We can use different cooling rates to sample a range of solidification conditions, collect the XRT data to capture the crystal growth *in-situ*, and then plot the change points from the cooling rate experiments in temperature-time space. The result should form a characteristic 'C-shaped' curve elucidating the phase transformation [1, 48]. Accurate diagrams can then inform processing conditions to achieve desired microstructures and properties.

Because this unsupervised binary classification algorithm does not require training data, it has potential for broad applications to other diffusive phase transformations including precipitation, spinodal decomposition, and coalescence. Knowledge of the underlying contrast mechanism and the rate of phase transformation will be paramount when testing the accuracy and stability of the detected critical point over multiple experimental datasets. Beyond *in-situ* X-ray studies of phase transformation, the authors hope the work can influence other fields that collect extended series of images over time (*i.e.*, medical or satellite imaging). Related to this point is the expansion of pixel-wide statistical measures that will allow for even greater flexibility when applied to various other scientific domains.

5 Conclusion

We introduce a three-step algorithm that is capable of identifying the critical event (such as nucleation) within a continuous image stream without requiring any training data. It does so by evaluating simple statistical metrics describing each frame in the dataset. The frame-wide data is subsequently reduced by principal component analysis and fuzzy clustered into pre- and post-nucleation regimes. The flexible unsupervised binary classification algorithm presented here has been tested on two juxtaposing experimental X-ray tomography datasets that record phase transformations in real-time: the rapid growth of a quasicrystal and the slow growth of a Si crytal from a melt. We verified the time sensitivity with respect to different solid growth rates *via* simulated phantoms and discovered that faster growth rates enable a more accurate detection of the nucleation time. We believe that this algorithm can be an additional tool for researchers to quickly screen image streams for critical events, from materials formation to materials failure.

References

[1] J. W. Christian. *The Theory of Transformations in Metals and Alloys*. Elsevier science, Dec. 10, 2002. 1202 pp. ISBN: 978-0-08-054277-5.

[2] Heike Emmerich. "Heterogeneous Nucleation and Microstructure Formation: From a Model Systems to Applied Metal Physics". In: *JOM* 66.8 (Aug. 1, 2014), pp. 1493–1495. ISSN: 1543-1851. DOI: 10.1007/s11837-014-1035-7.

[3] Frans Spaepen. "Homogeneous nucleation and the temperature dependence of the crystal-melt interfacial tension". In: *SOLID STATE PHYSICS-NEW YORK-ACADEMIC PRESS*- 47 (1994), pp. 1–1.

[4] Ashwin J. Shahani et al. "Characterization of metals in four dimensions". In: *Materials Research Letters* 8.12 (Dec. 1, 2020), pp. 462–476. ISSN: 2166-3831. DOI: 10.1080/21663831.2020.1809544.

[5] Philip J. Withers. "X-ray nanotomography". In: *Materials Today* 10.12 (Dec. 1, 2007), pp. 26–34. ISSN: 1369-7021. DOI: 10.1016/S1369-7021(07)70305-X.

[6] E. Maire and P. J. Withers. "Quantitative X-ray tomography". In: *International Materials Reviews* 59.1 (Jan. 1, 2014), pp. 1–43. ISSN: 0950-6608. DOI: 10.1179/1743280413Y.0000000023.

[7] Henri Nguyen-Thi et al. "On the interest of synchrotron X-ray imaging for the study of solidification in metallic alloys". In: *Comptes Rendus Physique*. Use of large scale facilities for research in metallurgy / Utilisation des grands instruments pour la recherche en métallurgie 13.3 (Apr. 1, 2012), pp. 237–245. ISSN: 1631-0705. DOI: 10.1016/j.crhy.2011.11.010.

[8] G. Reinhart et al. “In-Situ and Real-Time Analysis of the Formation of Strains and Microstructure Defects during Solidification of Al-3.5 Wt Pct Ni Alloys”. In: *Metallurgical and Materials Transactions A* 39.4 (Apr. 1, 2008), pp. 865–874. ISSN: 1543-1940. DOI: 10.1007/s11661-007-9449-2.

[9] Ashwin J. Shahani, Xianghui Xiao, and Peter W. Voorhees. “The mechanism of eutectic growth in highly anisotropic materials”. In: *Nature Communications* 7.1 (Sept. 27, 2016), pp. 1–7. ISSN: 2041-1723. DOI: 10.1038/ncomms12953.

[10] Saman Moniri, Xianghui Xiao, and Ashwin J. Shahani. “The mechanism of eutectic modification by trace impurities”. In: *Scientific Reports* 9.1 (Mar. 4, 2019), pp. 1–13. ISSN: 2045-2322. DOI: 10.1038/s41598-019-40455-3.

[11] Teng Zhou, Zhen Song, and Kai Sundmacher. “Big Data Creates New Opportunities for Materials Research: A Review on Methods and Applications of Machine Learning for Materials Design”. In: *Engineering* 5.6 (2019), pp. 1017–1026. ISSN: 2095-8099. DOI: https://doi.org/10.1016/j.eng.2019.02.011.

[12] Insung Han, Xianghui Xiao, and Ashwin J. Shahani. “Probing the growth and melting pathways of a decagonal quasicrystal in real-time”. In: *Scientific Reports* 7.1 (Dec. 12, 2017), pp. 1–10. ISSN: 2045-2322. DOI: 10.1038/s41598-017-17821-0.

[13] D. M. Herlach and B. Feuerbacher. “Non-equilibrium solidification of undercooled metallic melts”. In: *Advances in Space Research* 11.7 (Jan. 1, 1991), pp. 255–262. ISSN: 0273-1177. DOI: 10.1016/0273-1177(91)90293-S.

[14] Wenhao Sun and Gerbrand Ceder. “Induction time of a polymorphic transformation”. In: *CrystEngComm* 19.31 (Aug. 7, 2017). Publisher: The Royal Society of Chemistry, pp. 4576–4585. ISSN: 1466-8033. DOI: 10.1039/C7CE00766C.

[15] Doğa Gürsoy et al. “TomoPy: a framework for the analysis of synchrotron tomographic data”. In: *Journal of Synchrotron Radiation* 21 (Pt 5 Aug. 1, 2014), pp. 1188–1193. ISSN: 0909-0495. DOI: 10.1107/S1600577514013939.

[16] K. Aditya Mohan et al. “TIMBIR: A Method for Time-Space Reconstruction From Interlaced Views”. In: *IEEE Transactions on Computational Imaging* 1.2 (June 2015), pp. 96–111. ISSN: 2333-9403, 2334-0118. DOI: 10.1109/TCI.2015.2431913.

[17] Enzo Liotti et al. “Crystal nucleation in metallic alloys using x-ray radiography and machine learning”. In: *Science Advances* 4.4 (Apr. 1, 2018). Publisher: American Association for the Advancement of Science Section: Research Article, eaar4004. ISSN: 2375-2548. DOI: 10.1126/sciadv.aar4004.

[18] Samaneh Aminikhanghahi and Diane J. Cook. “A Survey of Methods for Time Series Change Point Detection”. In: *Knowledge and information systems* 51.2 (May 2017), pp. 339–367. ISSN: 0219-1377. DOI: 10.1007/s10115-016-0987-z. URL: https://www.ncbi.nlm.nih.gov/pmc/articles/PMC5464762/.

[19] Anthony Bagnall et al. “The great time series classification bake off: a review and experimental evaluation of recent algorithmic advances”. In: *Data Mining and Knowledge Discovery* 31.3 (May 1, 2017), pp. 606–660. ISSN: 1573-756X. DOI: 10.1007/s10618-016-0483-9.

[20] Carl S. Adorf et al. “Analysis of Self-Assembly Pathways with Unsupervised Machine Learning Algorithms”. In: *The Journal of Physical Chemistry B* 124.1 (Jan. 9, 2020). Publisher: American Chemical Society, pp. 69–78. ISSN: 1520-6106. DOI: 10.1021/acs.jpcb.9b09621.

[21] Betsy A. Dowd et al. “Developments in synchrotron x-ray computed microtomography at the National Synchrotron Light Source”. In: (Sept. 22, 1999). Ed. by Ulrich Bonse, pp. 224–236. DOI: 10.1117/12.363725.

[22] Guido Van Rossum and Fred L Drake Jr. *Python tutorial*. Centrum voor Wiskunde en Informatica Amsterdam, The Netherlands, 1995.

[23] F. Pedregosa et al. “Scikit-learn: Machine Learning in Python”. In: *Journal of Machine Learning Research* 12 (2011), pp. 2825–2830.

[24] Travis Oliphant. *NumPy: A guide to NumPy*. USA: Trelgol Publishing. 2006. URL: http://www.numpy.org/.

[25] The HDF Group. *Hierarchical Data Format, version 5*. http://www.hdfgroup.org/HDF5/. 1997-NNNN.

[26] Insung Han, Xianghui Xiao, and Ashwin J. Shahani. *Probing the growth and melting pathways of a decagonal quasicrystal in real-time*. 2017. DOI: 10.18126/M2K910. URL: https://petreldata.net/mdf/detail/pub_40_han_probing_v1.2.

[27] S. Moniri, X. Xiao, and A. J. Shahani. *Dataset for ”Singly-twinned growth of Si crystals upon chemical modification”*. 2020. DOI: 10.7302/812m-d307. URL: https://doi.org/10.7302/812m-d307.

[28] Paul Chao. *Sinogram Change Point Detection*. https://github.com/shahaniRG/sinogram_changepoint_detection. 2020.

[29] Lorenz Ratke and P. W Voorhees. *Growth and coarsening: Ostwald ripening in material processing*. OCLC: 751525888. Berlin; London: Springer, 2011. ISBN: 978-3-642-07644-2.

[30] MATLAB. *version 9.6.0 (R2019a)*. Natick, Massachusetts: The MathWorks Inc., 2019.

[31] W. Steurer. “Quasicrystals: What do we know? What do we want to know? What can we know?” In: *Acta Crystallographica Section A: Foundations and Advances* 74.1 (Jan. 1, 2018). Publisher: International Union of Crystallography, pp. 1–11. ISSN: 2053-2733. DOI: 10.1107/S2053273317016540.

[32] D. Holland-Moritz, D. M. Herlach, and K. Urban. “Observation of the undercoolability of quasicrystal-forming alloys by electromagnetic levitation”. In: *Physical Review Letters* 71.8 (Aug. 23, 1993), pp. 1196–1199. ISSN: 0031-9007. DOI: 10.1103/PhysRevLett.71.1196.

[33] Frederick Charles Frank and Nevill Francis Mott. “Supercooling of liquids”. In: *Proceedings of the Royal Society of London. Series A. Mathematical and Physical Sciences* 215.1120 (Nov. 6, 1952). Publisher: Royal Society, pp. 43–46. DOI: 10.1098/rspa.1952.0194.

[34] Jens Als-Nielsen and Des McMorrow. *Elements of Modern X-ray Physics*. 1st ed. Wiley, Mar. 18, 2011. ISBN: 978-0-470-97395-0. DOI: 10.1002/9781119998365.

[35] “Fundamentals of X-ray Physics”. In: *Computed Tomography: From Photon Statistics to Modern Cone-Beam CT*. Ed. by Thorsten Buzug. Berlin, Heidelberg: Springer, 2008, pp. 15–73. ISBN: 978-3-540-39408-2. DOI: 10.1007/978-3-540-39408-2_2.

[36] Jake Lever, Martin Krzywinski, and Naomi Altman. “Principal component analysis”. In: *Nature Methods* 14.7 (July 1, 2017), pp. 641–642. ISSN: 1548-7105. DOI: 10.1038/nmeth.4346.

[37] Brian S. Everitt et al. *Cluster Analysis*. 5 edition. Chichester, West Sussex, U.K: Wiley, Feb. 21, 2011. ISBN: 978-0-470-74991-3.

[38] Slawomir Wierzchon and Mieczyslaw Klopotek. *Modern Algorithms of Cluster Analysis*. Studies in Big Data. Springer International Publishing, 2018. ISBN: 978-3-319-69307-1. DOI: 10.1007/978-3-319-69308-8.

[39] James C. Bezdek, Robert Ehrlich, and William Full. “FCM: The fuzzy c-means clustering algorithm”. In: *Computers & Geosciences* 10.2 (Jan. 1984), pp. 191–203. ISSN: 00983004. DOI: 10.1016/0098-3004(84)90020-7.

[40] N.R. Pal and J.C. Bezdek. “On cluster validity for the fuzzy c-means model”. In: *IEEE Transactions on Fuzzy Systems* 3.3 (Aug. 1995). Conference Name: IEEE Transactions on Fuzzy Systems, pp. 370–379. ISSN: 1941-0034. DOI: 10.1109/91.413225.

[41] Yoshihiko Yokoyama et al. “Preparation of Decagonal Al–Ni–Co Single Quasicrystal by Czochralski Method”. In: *Materials transactions, JIM* 38.11 (1997), pp. 943–949.

[42] Saman Moniri, Xianghui Xiao, and Ashwin J. Shahani. “Singly-twinned growth of Si crystals upon chemical modification”. In: *Physical Review Materials* 4.6 (June 19, 2020). Publisher: American Physical Society, p. 063403. DOI: 10.1103/PhysRevMaterials.4.063403.

[43] Hans Leo Lukas and Nathalie Lebrun. “Aluminium – Copper – Silicon”. In: *Landolt-Börnstein - Group IV Physical Chemistry* 11A2 (), p. 13. DOI: 10.1007/10915967_9.

[44] R. H. Mathiesen et al. “X-Ray Videomicroscopy Studies of Eutectic Al-Si Solidification in Al-Si-Cu”. In: *Metallurgical and Materials Transactions A* 42.1 (Jan. 1, 2011), pp. 170–180. ISSN: 1543-1940. DOI: 10.1007/s11661-010-0443-8.

[45] Jiang Hsieh. *Computed tomography principles, design, artifacts, and recent advances*. Bellingham, Washington: SPIE, 2015. ISBN: 978-1-62841-825-5.

[46] J-O Andersson et al. “Thermo-Calc & DICTRA, computational tools for materials science”. In: *Calphad* 26.2 (June 1, 2002), pp. 273–312. ISSN: 0364-5916. DOI: 10.1016/S0364-5916(02)00037-8.

[47] D. R. Hamilton and R. G. Seidensticker. “Propagation Mechanism of Germanium Dendrites”. In: *Journal of Applied Physics* 31.7 (). Publisher: American Institute of Physics, pp. 1165–1168. ISSN: 0021-8979. DOI: 10.1063/1.1735796. (Visited on 07/13/2020).

[48] David A. Porter and Kenneth E. Easterling. *Phase Transformations in Metals and Alloys, Third Edition (Revised Reprint)*. Google-Books-ID: eYR5Re5tZisC. CRC Press, Sept. 10, 1992. 532 pp. ISBN: 978-0-7487-5741-1.

[49] Naji S. Husseini et al. “Mapping single-crystal dendritic microstructure and defects in nickel-base superalloys with synchrotron radiation”. In: *Acta Materialia* 56.17 (Oct. 1, 2008), pp. 4715–4723. ISSN: 1359-6454. DOI: 10.1016/j.actamat.2008.05.041.

[50] I. Han et al. “A side-by-side comparison of the solidification dynamics of quasicrystalline and approximant phases in the Al–Co–Ni system”. In: *Acta Crystallographica Section A: Foundations and Advances* 75.2 (Mar. 1, 2019). Number: 2 Publisher: International Union of Crystallography, pp. 281–296. ISSN: 2053-2733. DOI: 10.1107/S2053273318017114.

Figure Captions

Fig. 1 (a) Illustration of the experimental set-up for *in situ* X-ray tomography. Forward transmitted partially coherent X-rays pass through a rotating sample and are collected on a two dimensional detector (where coordinates r_1 and r_2 define the detector plane). These projections are collected continuously over a range of rotation angles θ for the duration of the experiment. (b) Processed, downsampled (by a factor of 10), and normalized sinogram for case study #1. The apparent contrast change is the result of quasicrystal formation. 200 timesteps is equivalent to a 360° sample rotation and a time period of 80 seconds

Fig. 2 Trends in maximum value, mean value, median value, standard deviation and other measures of central tendency over the experimental duration. The abscissa indicates the computed result for each projection (or column vector in Fig. 5(b)); note again that 200 projections correspond to a 360° rotation of the sample and a time period of 80 seconds. The ordinate reflects data discretized to 256 levels

Fig. 3 Results on data reduction and clustering for case study #1. (a) Principal component analysis (PCA), where each point represents a given projection (column vector in Fig. 5(b)), colored by time. The clustered orthographic projection is colored such that red indicates those projections that fall in the pre-nucleation regime and blue the converse. (b) The colored, clustered orthographic projection is shown with arrows drawn from the coordinate origin showing the degree to which each metric (in Fig. 5) contributes to the PCA result. Each arrow in the biplot is labeled and its magnitude and direction indicate the variance captured in the first and second principal component. (c) Likelihood of cluster membership determined by fuzzy clustering. The result is smoothed with a median filter (the window size equal to a period in the sinogram) and superimposed. The intersection of the cluster memberships is the estimated change point

Fig. 4 Results on data reduction and clustering for case study #2. (A) Processed sinogram downsampled by a factor of 10 such that every 300 time units is equal to a 360° sample rotation and a time period of 42 s. Thin dark lines which are visible just after 5,000 time units correspond to the nucleation and growth of the Si crystals. (B) 3D scatter plot of the two primary principal components and time with the clustered result colored in the orthographic projection. Clusters are less distinct compared to Fig. 5 but the nucleation time is still adequately estimated by the (C) fuzzy clustering algorithm, by comparing to the sinogram shown in (a)

Fig. 5 Comparison of simulated phantoms under (a) slow and (b) fast growth rates. The green arrow in the simulated sinogram (top) indicates the imposed nucleation event and that in the fuzzy probability plot (bottom) indicates the estimated critical point. The same measures of central tendency listed in Fig. 2 were used to quantify changes between the columns of the sinograms

6 Supplemental information

6.1 Downsampling factor

Detected nucleation point with respect to downsampling factor is shown below. The downsampling factor is defined as the neighborhood size that is combined (*e.g.*, for a downsampling factor of 10×, the downsampled sinogram will be the sum total of 10×10 pixels in the original sinogram with no overlap). The detected nucleation time-step is well within the 180° period in the sinogram (1,000 projections or time-steps).

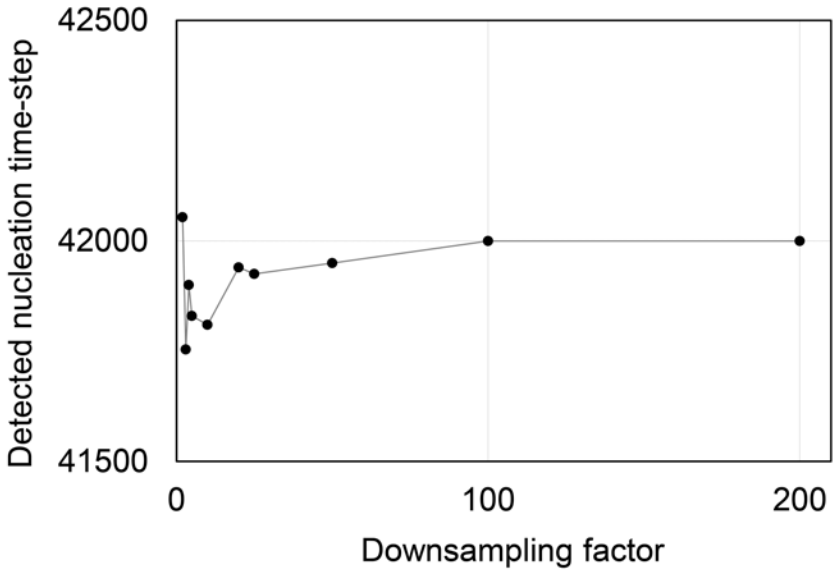

6.2 PCA Scree plot

Scree plot showing the amount of variance captured along each principal component. For case study #1, 87.96% of the aggregate variance is captured with two principal components.

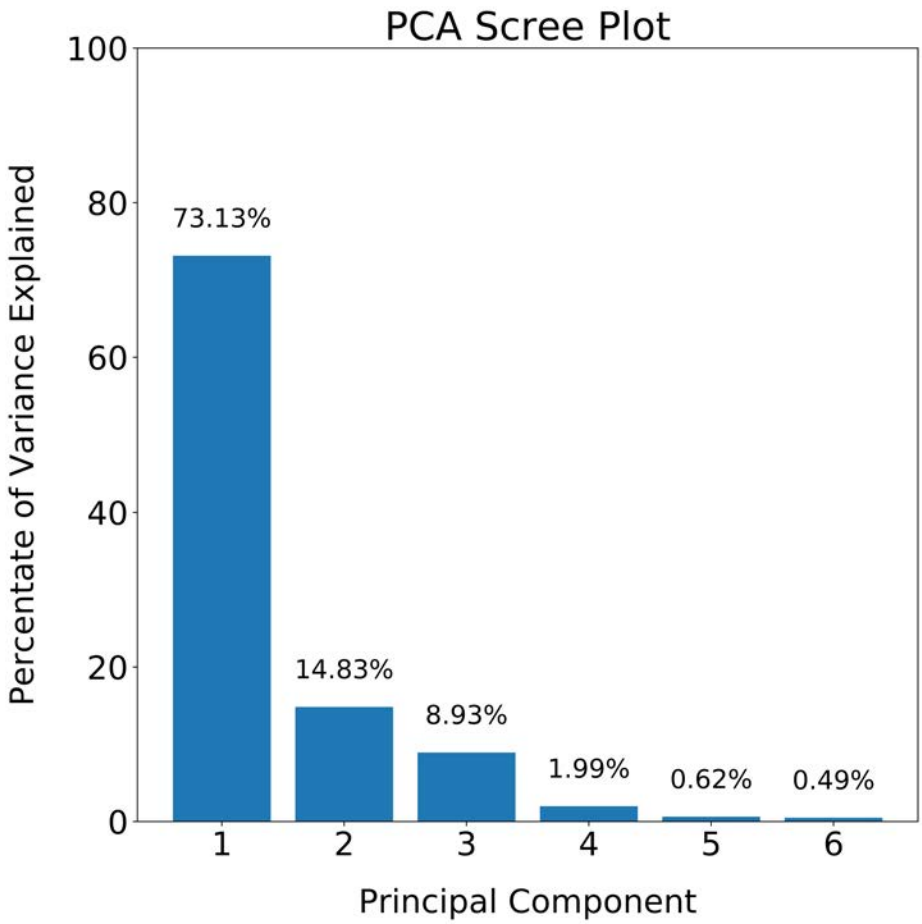

6.3 Case study # 1: 3D reconstructions

Volume reconstructions of the quasicrystal (in red) upon solidification from a liquid. Shown are the 40-45th reconstructed volumes in a dynamic X-ray tomography experiment, corresponding to 800 seconds (1259.8 K) to 1000 seconds (1256.5 K). Each reconstruction covers a time-interval of 40 seconds (0.67 K) [12]. The quasicrystal grows quickly from one side of the sample to the other by the 41th reconstructed volume. The sample diameter is 1 mm.

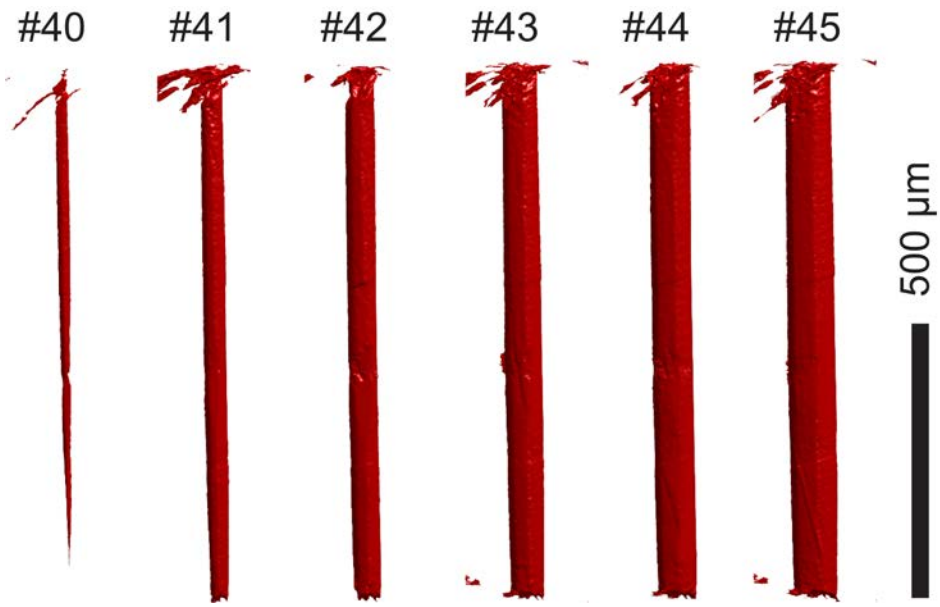

6.4 Case study # 2: 3D reconstructions

Volume reconstructions of the Si crystal (red) upon solidification from a liquid [42]. The entirety of the sample within the tomographic field-of-view (grey) is included to show scale and perspective for the two crystals. Depicted are the renderings of the 45th, 50th, 55th and 60th volumes in a dynamic X-ray tomography experiment. The Si emerges in the 45th reconstruction corresponding to 22.5 min (1185 K). The 60th reconstruction corresponds to 35.5 min (1172 K).

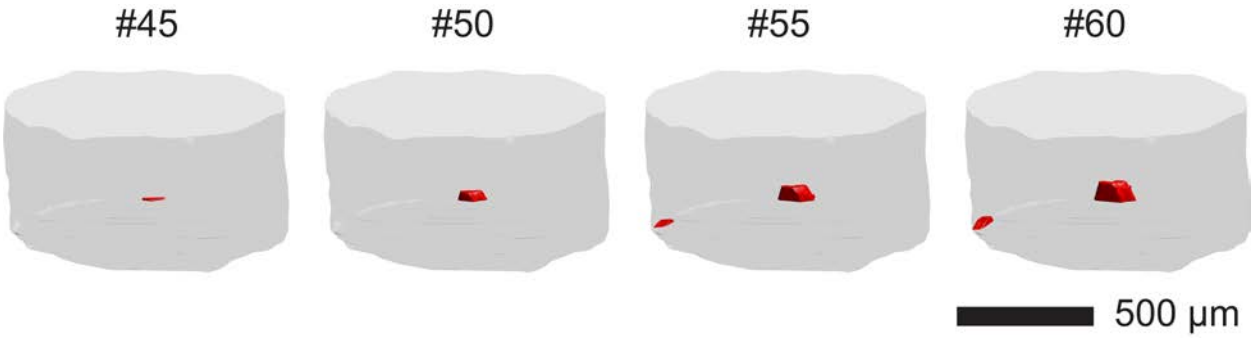

6.5 Details of simulation procedure

This simulation was constructed in MATLAB R2019a [30] by specifying a two dimensional array with values in the range of [0, 1] indicating the fractional composition of an element in a binary alloy. We constructed a 500×500 unit array containing a 400 unit diameter circle representing the sample. We nucleated a solid phase to model the evolution of the system from a *liquid* state to a *liquid* + *solid* state. The simulation allows the user to define the phantom attributes and most importantly choose the nucleation time-step, as will be described below.

There are two sets of parameters the user may control. The first is related to the alloy system and growth kinetics of the solid phase: the initial composition of the liquid (*i.e.*, the alloy composition), the equilibrium partition coefficient, maximum solid size and characteristic diffusion time (which scales inversely with the liquid diffusivity and the initial supersaturation in the liquid) [29]. The second set of parameters is related to the phantom projection: the elemental attenuation coefficient and data acquisition rate (*i.e.*, revolution rate or the angle increment per time-step).

The simulation takes these parameters to define the initial state of the phantom. At each time-step, the simulated phantom is rotated in-plane (*e.g.*, for 5°/time-step, the phantom is rotated by a cumulative angle of 50°at the 10^{th} time-step). The forward projection is calculated from the rotated phantom by taking the line integral along the path of the beam [49]. Denote the pixel-wide fractions of elements A and B as f_A and f_B, respectively, and the spatial coordinates of the rotated phantom as x and y. Then, the projected intensity in the y direction can be found as

$$I(x) = I_o \exp\left(-\mu_A \sum_{i=1}^{y} f_A(x,i) - \mu_B \sum_{i=1}^{y} f_B(x,i)\right) \tag{1}$$

where μ_A and μ_B are the attenuation coefficients of elements A and B, respectively, and I_0 is the intensity of the incident beam. Note $f_A + f_B = 1$ for the binary alloy so considered. Any positive integer for I_0 will suffice as the sinogram is later normalized. The column vector $I(x)$ represents a one dimensional projection of a two dimensional domain. The projections collected at different view angles are combined to yield the sinogram, as described in the main text.

When the simulation progresses to the chosen nucleation time-step, a solid phase is 'seeded' at an arbitrary location in the sample. The composition of the solid phase is determined by the equilibrium partition coefficient and the liquid composition. The radius of the growing circular solid phase is defined by eqn. 2 assuming that the supersaturation is not constant but instead decays in time as the solid grows [29]: this analytical solution best represents our solidification experiments [12, 50] which reveal that growth slows down upon prolonged annealing as the supersaturation is gradually relieved.

$$\frac{1}{6}\ln\left(\frac{1+\hat{r}+\hat{r}^2}{(1+\hat{r}^2)}\right) - \frac{1}{\sqrt{3}}\left(\arctan\left(\frac{2\hat{r}+1}{\sqrt{3}}\right) + \arctan\left(\frac{1}{\sqrt{3}}\right)\right) = \frac{t}{\tau} \tag{2}$$

Note that the solid radius $\hat{r}$ is normalized against its maximum size, the time t is zero when the solid nucleates, and the characteristic diffusion time τ determines the rate at which the solid grows [29]. Here we treat t as the simulation time-step and we then solve for $\hat{r}$ to update the simulation accordingly. The characteristic diffusion time τ is the last remaining physical parameter that is input in our simulation. Following the nucleation and growth of the solid, the liquid composition is updated accordingly to reflect a conservation of mass. This is done by distributing the remaining amount of solute not in the solid to the liquid phase (*i.e.* solute rejection). Ultimately, the unscaled solid radius is a function of the simulation time-step and the user-defined maximum radius size (100 units is chosen as default, resulting in a 60% solid area when growth is complete). With these parameters, the solid phase does not touch the

boundaries of the simulation domain.

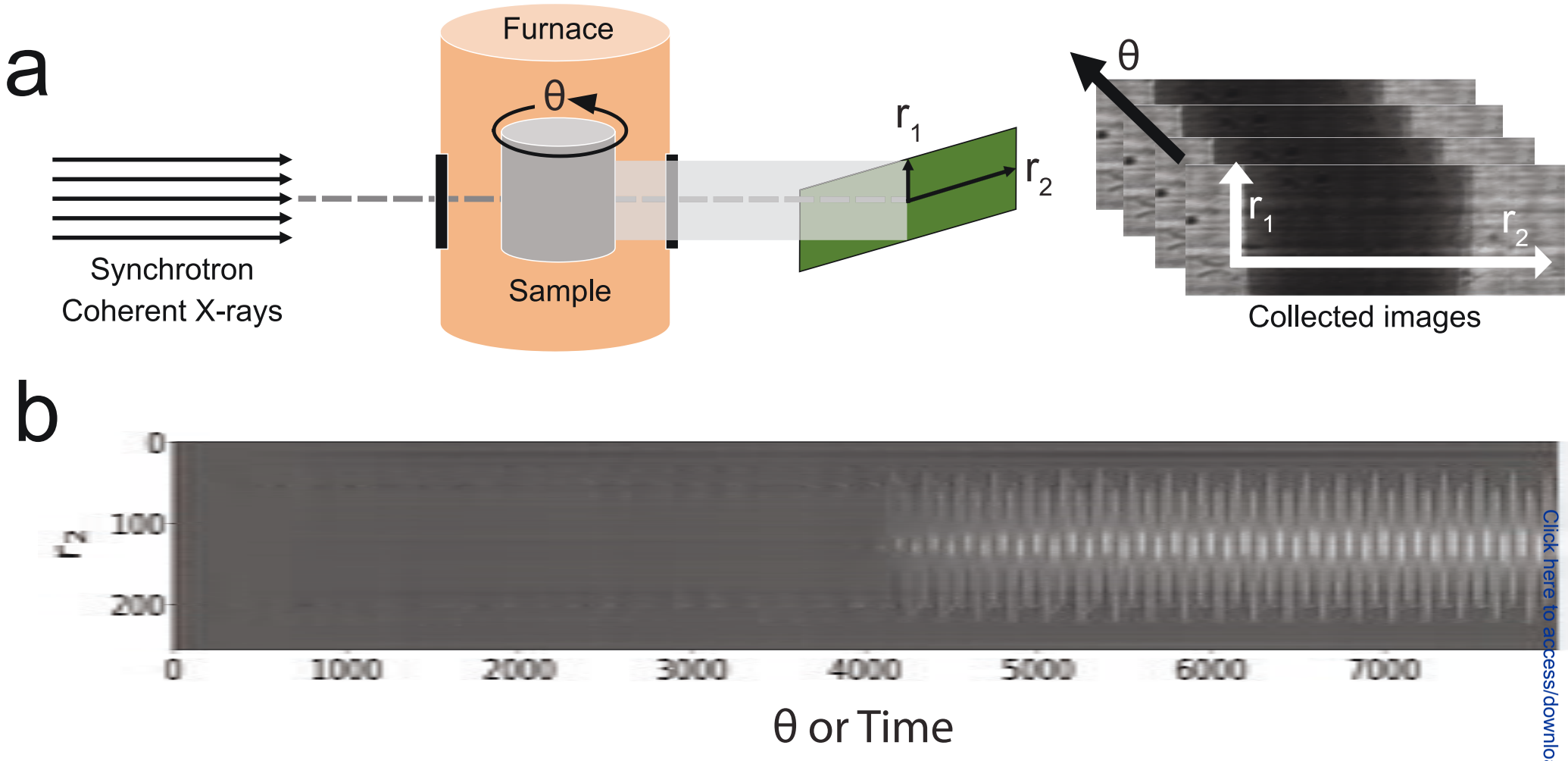

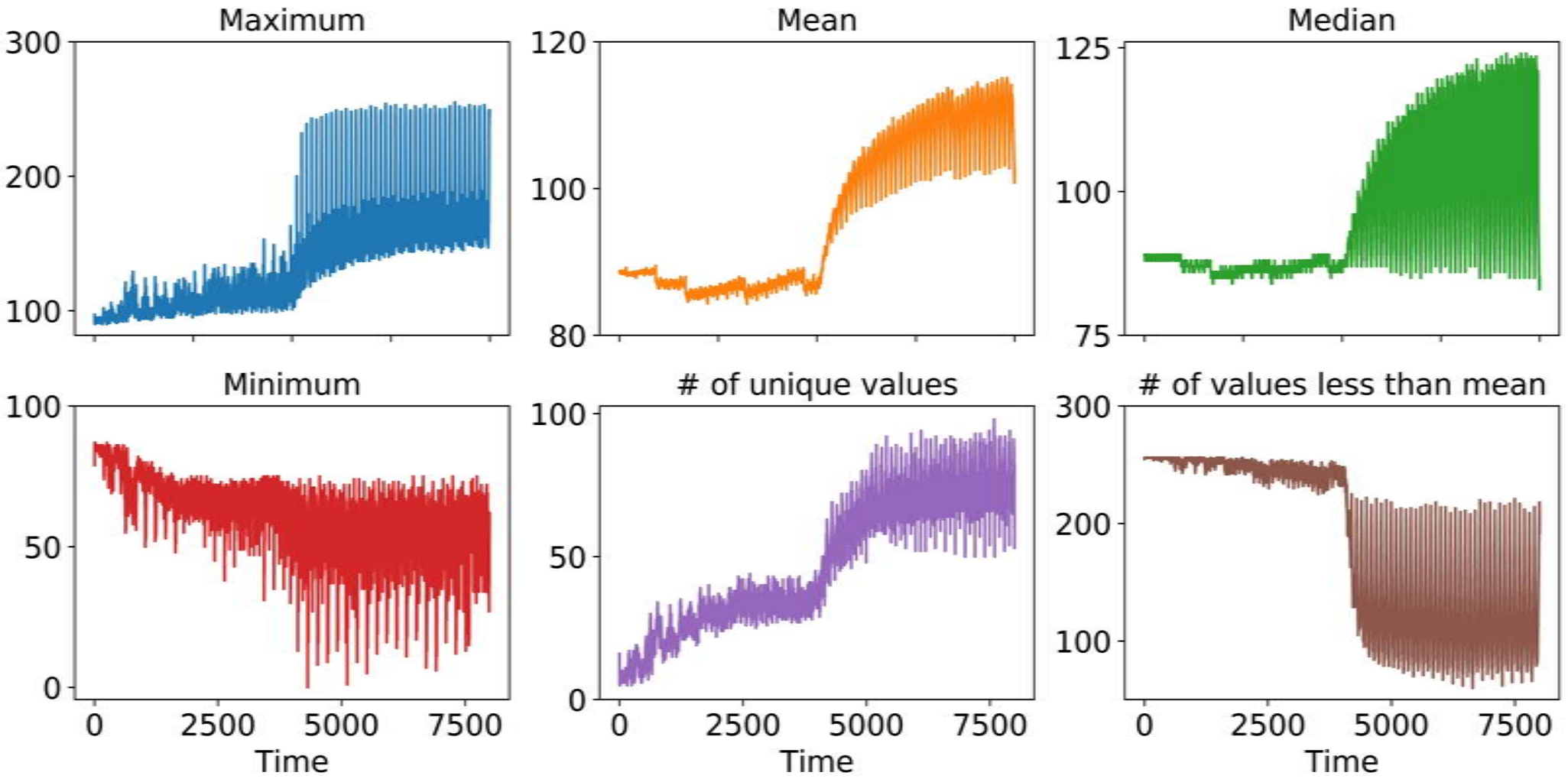

Figure

Click here to access/download;Figure;Fig3.eps

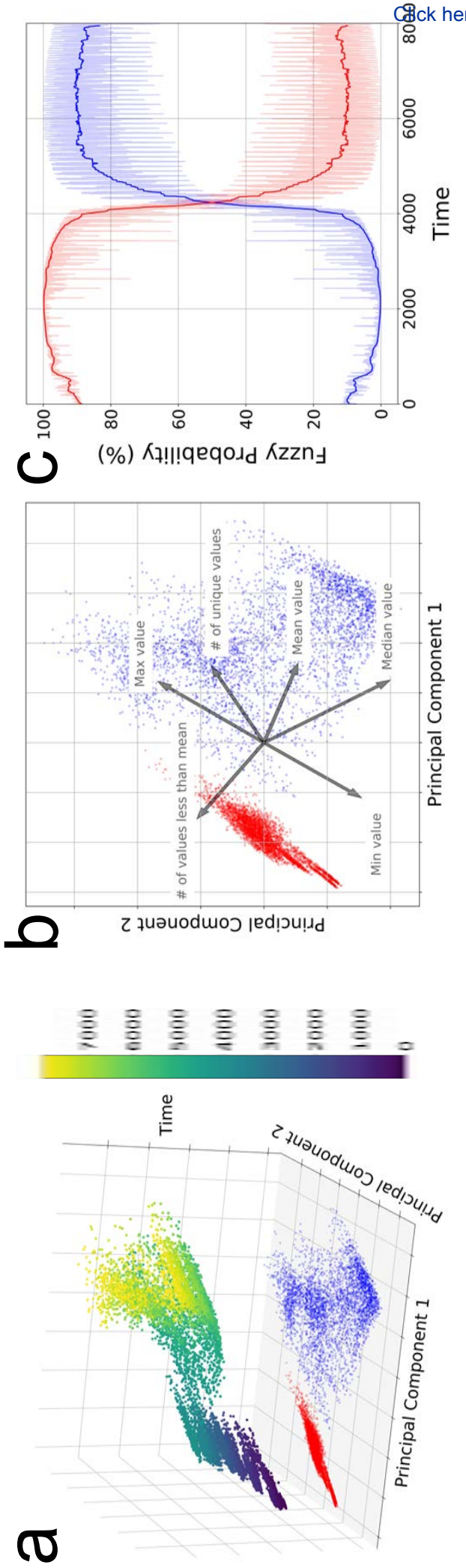

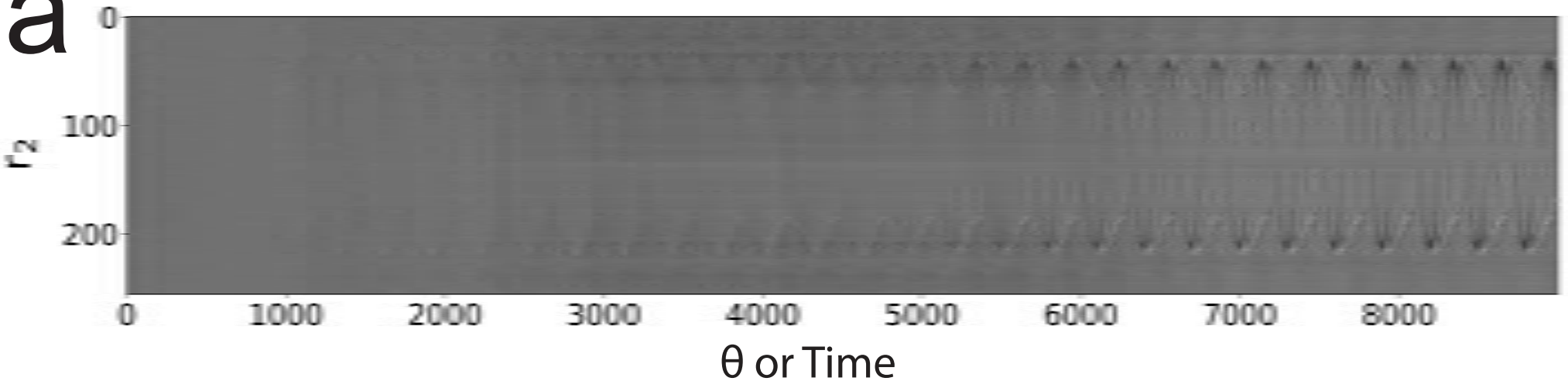

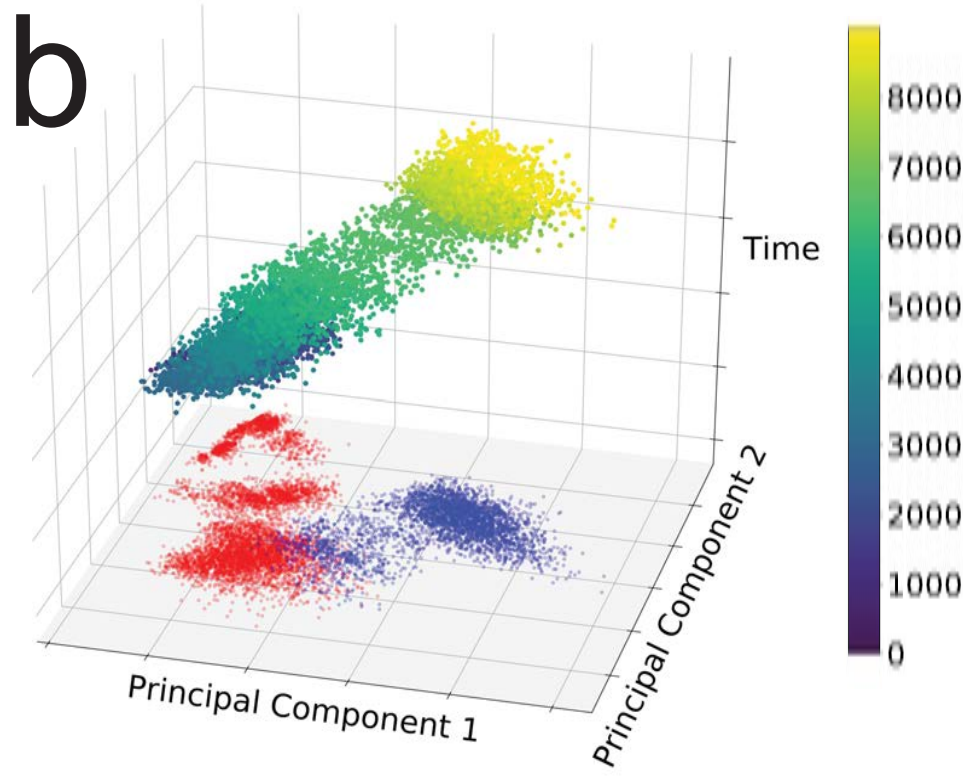

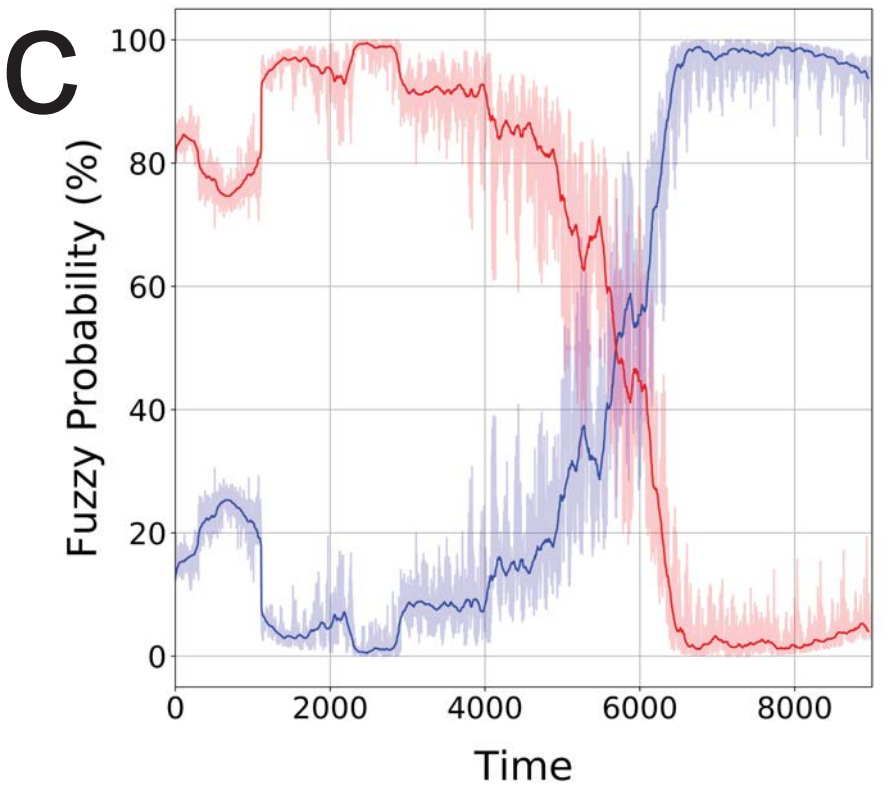

Figure

Click here to access/download;Figure;Fig5.eps